Check for updates

Brian R. Elbing[1]
Mem. ASME
School of Mechanical and Aerospace Engineering,
Oklahoma State University,
201 General Academic Building,
Stillwater, OK 74078
e-mail: elbing@okstate.edu

Steven D. Young
Mem. ASME
Applied Research Laboratory,
Pennsylvania State University,
3210B Garfield Thomas Water Tunnel,
University Park, PA 16802
e-mail: sdy101@psu.edu

Michael L. Jonson
Mem. ASME
Applied Research Laboratory,
Pennsylvania State University,
3200B Garfield Thomas Water Tunnel,
University Park, PA 16802
e-mail: mxj6@psu.edu

Robert L. Campbell
Mem. ASME
Applied Research Laboratory,
Pennsylvania State University,
300R Garfield Thomas Water Tunnel,
University Park, PA 16802
e-mail: rlcampbell@psu.edu

Brent A. Craven[2]
Applied Research Laboratory,
Department of Mechanical and Nuclear Engineering,
Pennsylvania State University,
University Park, PA 16802
e-mail: brent.craven@fda.hhs.gov

Robert F. Kunz
Mem. ASME
Department of Mechanical and Nuclear Engineering,
Pennsylvania State University,
301C Reber Building,
University Park, PA 16802
e-mail: rfk102@psu.edu

Kevin L. Koudela
Applied Research Laboratory,
Pennsylvania State University,
155 Applied Research Laboratory,
University Park, PA 16802
e-mail: klk121@psu.edu

Experimental Characterization of High-Amplitude Fluid–Structure Interaction of a Flexible Hydrofoil at High Reynolds Number

A fluid–structure interaction (FSI) experiment was performed to study low-frequency (~10 Hz), high-amplitude (±3.5% of the span) fin motion. This was achieved by placing an Inconel swept-fin at −9.6 deg angle-of-attack within the wake of a roughened cylinder. Speeds between 2.5 and 3.6 m/s produced cylinder diameter-based Reynolds numbers between 190,000 and 280,000, respectively. Detailed descriptions of the geometry, material/structural behavior, fluid properties, and initial conditions are provided to facilitate computational model development. Given the initial conditions, the resulting forced fin behavior was characterized with measurements of the mean and fluctuating velocity upstream of the fin (i.e., within the cylinder wake), fin tip/surface motion, and fin constraint forces/moments. This work provides a detailed experimental dataset of conditions mimicking a crashback event that is also a challenging FSI benchmark problem involving turbulent, vortex-induced structure motion. It has been used as a validation condition for FSI simulations, and it can be used to validate other FSI models as well as identifying strengths and weaknesses of various modeling approaches. [DOI: 10.1115/1.4046751]

Keyword: flow-induced noise and vibration

Downloaded from http://asmedigitalcollection.asme.org/vibrationacoustics/article-pdf/142/4/041014/6527766/vib_142_4_041014.pdf by guest on 23 April 2024

1 Introduction

When a fluid flows over an object, it imparts stresses on the structure, which if sufficiently large can deform the structure and/or move it such that it modifies the flow pattern and consequently alters the stresses on the structure. Fluid–structure interaction (FSI) modeling aims to capture the interaction between the structure and the flow. Aerospace and marine applications are particularly interested in FSI modeling since lightweight and composite materials offer long life, high strength, and reduced weight while also producing significant FSI in unsteady flows. One of the most extreme operating conditions experienced by a ship or submarine propeller

[1]Corresponding author.
[2]Present address: Division of Applied Mechanics, Office of Science and Engineering Laboratories, Center for Devices and Radiological Health, U.S. Food and Drug Administration, Silver Spring, MD 20993.

Contributed by the Design Engineering Division of ASME for publication in the Journal of Vibration and Acoustics. Manuscript received August 12, 2019; final manuscript received February 26, 2020; published online March 26, 2020. Assoc. Editor: Maurizio Porfiri.

 Copyright © 2020 by ASME

is a *crashback* maneuver [1–5], which occurs when a forward moving vessel reverses the propeller rotation to quickly stop. Development of computational tools to accurately predict the maximum stresses and deflections during crashback would significantly improve the propeller design process. Modeling of crashback events for traditional propulsors has been an open research topic for years [6–9]. This problem will become even more important as the use of composite materials [10–13] and new propulsion schemes [14–16] are explored. Improving crashback modeling capabilities was the focus of a companion paper [17] to the current study, which provides experimental results from a fin subjected to high-amplitude, flow-induced oscillations to mimic crashback conditions.

Ideally, the model would be two-way coupled such that the fluid and structure can affect one another. Interest in two-way coupled models has recently increased due to computational advances, maturing of flow/structural modeling, and realization of potential applications. While there is a large body of work related to small deformation, dynamic aeroelastic/hydroelastic modeling (e.g., flutter [18,19], vortex-induced vibrations [20–23]), there is a dearth of FSI literature when the structure experiences large deformations as observed with crashback. Campbell and Paterson [24] reviews the available literature and presents a method for computing pump performance with highly flexible impellers. Flexible turbomachinery has gained interest among researchers [25–28] due to the deformable structure aiding implantation for biomedical applications. In this application, the structural response and the fluid flow are strongly coupled due to the large flow-induced deformations, which require that the fluid flow and structural response be solved simultaneously. See Heil and Hazel [29] for a review of FSI-related internal physiological flows, and Dowell and Hall [30] for a review of FSI modeling approaches.

FSI models advancement has been limited, in part, due to the challenge of performing unsteady flow experiments that are strongly coupled with structural motions/deformation with sufficient accuracy needed for FSI model validation (e.g., Ref. [31]). One approach is to use a rigid fin oscillating in a controlled manner but mounted on a flexible base such that the fin can shift from the flow-induced loading [32–34]. An alternative approach is to mount a flexible membrane within a cylinder wake, which tip deflections and velocities from this approach have been reported up to a Reynolds number of 500 [35]. A similar study at higher Reynolds number (3.0×10^4) [36] is one of the few turbulent FSI test cases.

The current study performs a similar experiment, but instead of a flexible membrane, a fin was mounted in the cylinder wake to mimic crashback. The cylinder was sized to induce fin angle-of-attack variations at a frequency such that a quasi-steady lift varied by nominally 40%. In addition, the flow was turbulent with a cylinder Reynolds number up to 2.8×10^5. Measurements included two-component velocity in the wake, surface deflections, and constraint forces and moments on the fin. This study fills a void in the literature for high-fidelity, fully coupled FSI experiments with large structural deformations. A comparison between this study and a tightly coupled FSI simulation is available [17].

2 Experimental Methods

2.1 Test Facility and Configuration. Testing was done in the Applied Research Lab 12-in. water tunnel [37,38]. The test section was 760 mm long with a circular cross section. To minimize acceleration from boundary layer growth, the diameter gradually increased from 305 mm (12-in.) at the inlet to 307 mm at the outlet. The empty test section freestream turbulence intensity was <0.3%. The test configuration was a backward-facing fin (to mimic crashback) mounted in the wake of a 60 mm diameter circular cylinder as shown in Fig. 1. The contraction upstream of the test section had an 8.9:1 area ratio, 1.5 m long and a fifth-order polynomial shape [39]. The coordinate system has the x-axis increasing in the streamwise direction with its origin at the cylinder center. The

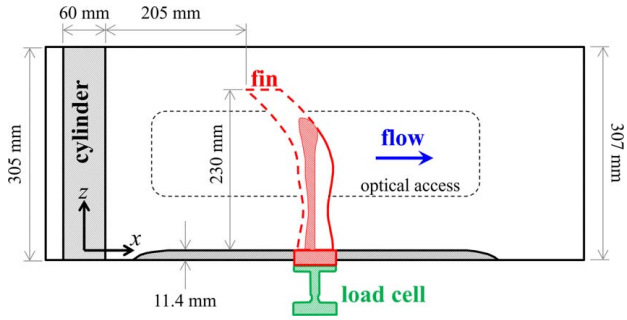

Fig. 1 Cross-sectional view at $y = 0$ of the test section. The fin was rotated 9.6 deg about the z-axis, which corresponds to $\alpha = -9.6$ deg. Optical access was 465 mm long and 120 mm high.

z-axis increases vertically upward with the origin at the fin base, which was 11.4 mm above inlet floor due a ramp used to make a flat surface for fin mounting (see Fig. 1). The elliptical shaped ramp spanned $x = 70$ mm to $x = 119$ mm. The y-axis completes a right-handed coordinate system with the origin at the tunnel centerline. Technical drawings and IGES files for the test section are in the Supplemental Material on the ASME Digital Collection.

2.2 Test Model. The anodized aluminum cylinder spanned the test section height with its axis of rotation (centerline) at $(x,y) = (0,0)$. The cylinder leading edge was roughened between $\theta = \pm 50$ deg with 254 μm mean diameter silicon carbide grit, where θ is the angular position from the leading edge (see Fig. 2). This roughness was selected based on past work [40] that showed that the base coefficient and Strouhal number were Reynolds number independent. The cylinder was instrumented with four dynamic pressure (dp) transducers (105C02, PCB) and two static pressure (sp) ports. The dp transducers were located at $\theta = \pm 130$ deg at the fin tip ($z = 230$ mm) and mid-span ($z = 115$ mm) heights (see Fig. 2). Static ports were at the same heights and $\theta = 180$ deg. An accelerometer (303M231, PCB) was mounted in the cylinder.

The fin base must move freely to measure constraint forces. Typically, a load cell (LC) uses a stiff model with a small gap between the model and the surrounding structure (e.g., Ref. [41]), but the large flow-induced motion required a larger gap. In addition, the load cell flexure was weakened to improve sensitivity, which required the fin and load cell assembly to be considered as the FSI test article. The fin, including a 23 mm thick base, was machined from a single piece of Inconel 718. It had a 49.5 mm chord, 230 mm span, average surface roughness <1.6 μm, and was swept forward (to mimic crashback) 75 mm. The angle-of-attack (α) was fixed at −9.6 deg, which produced ~3% solid blockage. The fin cross section was a NACA 4408 profile. From the base to mid-span, the fin was straight and necked down to a minimum chord of 35 mm at 25% span. Table 1 provides leading and trailing edge locations, chord length, and α along the span. The load cell was fabricated from beryllium copper with dimensions shown in Fig. 2. The technical drawings and IGES files for the fin (and load cell) are provided in the Supplemental Material on the ASME Digital Collection.

Static testing was done by applying point loads to the fin at 75% span and 62% chord (denoted by "×" in Fig. 2) with and without the load cell. The fin tip deflection (δ_t) versus applied force (gradual ramp or static) is shown in Fig. 3. The slopes for the fin only and fin with LC are 0.104 mm/N and 0.190 mm/N, respectively. The mode shapes and loss factors were determined from in-air and in-water modal impact tests with a roving hammer and accelerometers. Mode shapes, resonance frequencies, and loss factors were identified using a singular value decomposition approach combined with rational fraction polynomial curve fitting [42]. The frequency and loss factors of the first seven modes in-air and in-water are provided in Table 2.

Downloaded from http://asmedigitalcollection.asme.org/vibrationacoustics/article-pdf/142/4/041014/6527766/vib_142_4_041014.pdf by guest on 23 April 2024

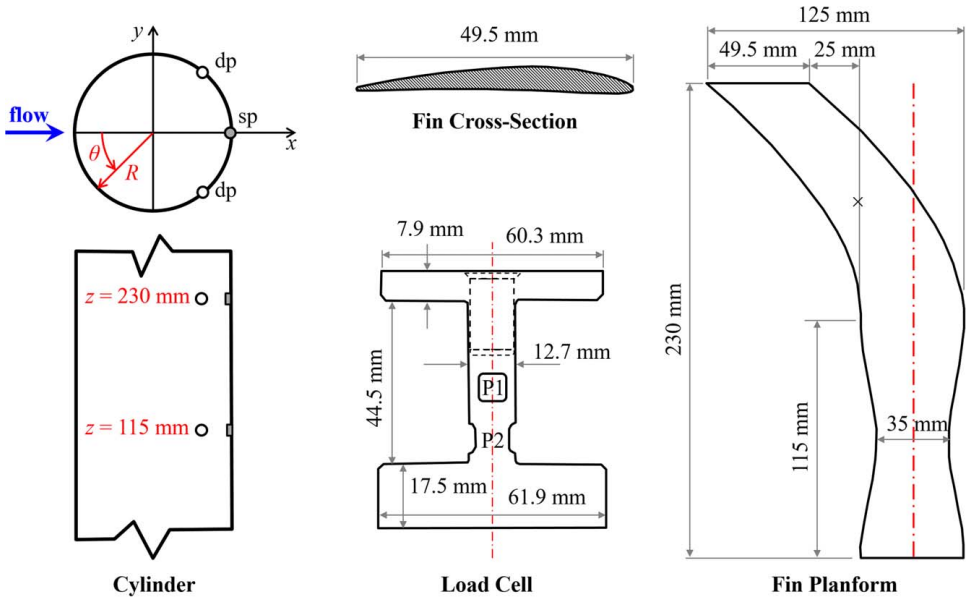

Fig. 2 Sketches of the cylinder, load cell, and fin (without the mounting base). Dynamic and static pressure measurements are denoted by "dp" and "sp," respectively. The drag (P1) and lift (P2) force pockets are shown. Centerlines indicate the fin and load cell axes of rotation.

Table 1 Laser scanning results of as-built fin, including position of the leading/trailing edges, chord length, and installed angle-of-attack (average $\alpha = -9.64$ deg)

	Leading edge		Trailing edge			
Span (%)	x (mm)	y (mm)	x (mm)	y (mm)	Chord (mm)	a (deg)
1.5	310.2	−5.2	359.2	3.0	49.7	−9.50
11	313.4	−4.7	356.1	2.7	43.3	−9.83
21	317.1	−3.9	352.4	2.0	35.8	−9.49
31	316.3	−4.0	353.1	2.4	37.4	−9.87
41	312.1	−4.6	357.1	3.2	45.7	−9.83
51	309.8	−4.9	359.0	3.5	49.9	−9.69
61	305.4	−5.4	354.4	3.0	49.7	−9.73
70	295.8	−6.7	344.7	1.5	49.6	−9.52
78	283.0	−8.8	331.8	−0.5	49.5	−9.65
86	268.2	−11.3	316.9	−3.0	49.4	−9.67
93	252.1	−13.8	300.7	−5.5	49.3	−9.69
100	235.4	−16.3	283.6	−8.5	48.8	−9.19

Table 2 Frequency and loss factors for the first seven vibration modes from the modal test of the model in the water tunnel

Mode number	Description	Frequency (Hz)		Loss factor	
		In-air	In-water	In-air	In-water
1	First cross-stream bending	32.7	23.2	0.003	0.011
2	First streamwise bending	44.7	43.9	0.005	0.009
3	Second cross-stream bending	132.0	103.0	0.004	0.007
4	First torsion	213.0	185.0	0.015	0.009
5	Third cross-stream bending	318.0	285.0	0.002	0.005
6	Second streamwise bending	371.0	341.0	0.036	0.059
7	Second torsion	587.0	462.0	0.012	0.021

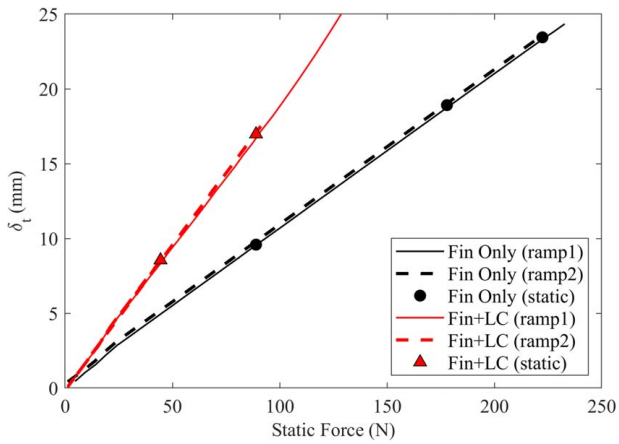

Fig. 3 Fin tip deflection (δ_t) with and without the load cell (LC) with a gradual ramp or static loading

2.3 Instrumentation. Two-component (x and y) particle image velocimetry (PIV) was acquired at $z = 188$ mm. The image plane was illuminated with a laser sheet formed with an Nd:YLF diode pumped laser (DM50-527, Photonics Industries). Scattered light from 18 μm diameter tracer particles (iM30 K, 3 M) were imaged with a 1280×800 pixel CMOS camera (v1610, Phantom). A minimum of 3000 image pairs were acquired per condition at 1 kHz. The field-of-view spanned $x = 100$–340 mm and $y = -80$ to 85 mm. Vectors were computed using standard multiple pass, cross-correlation (DaVis 8, LaVision) with a final interrogation window of 24×24 pixels with 75% overlap (1.4 mm vector spacing). A subset of conditions used laser Doppler velocimetry (LDV), which used an argon ion laser (Innova 70C-5, Coherent) coupled to a fiber optic probe head (9832, TSI) fitted with a 350 mm lens (9253-350, TSI Incorporated). The nominal measurement volume was 1.5 mm (length) by 150 μm (diameter) [43]. Most conditions acquired 20,000 samples per component.

The fin motion and orientation were monitored with a rotary encoder and an optical switch [44]. For a subset of conditions, high-speed imaging provided fin tip deflection (translational motion) and twist (rotational motion). The motion was identified via

Downloaded from http://asmedigitalcollection.asme.org/vibrationacoustics/article-pdf/142/4/041014/6527766/vib_142_4_041014.pdf by guest on 23 April 2024

cross-correlation between an image and a reference (no-flow) image, which was confirmed with 400 manually inspected images. This also showed that the unloaded fin tip position varied <10 μm (1 pixel) throughout testing. The fin surface velocity was measured with a laser vibrometer (PSV-400-3D, Polytec) at 21 locations (7 × 3 grid; 40, 50, 60, 70, 80, 90, 95% span; 10, 50, 90% chord) and integrated to get displacements. The beam was perpendicular to the fin surface at 90% chord with no-flow ($\alpha = -9.6$ deg) and corrections for relative surface angle at each location were applied. A reference vibrometer (OFV-505/5000, Polytec) was fixed at 80% span, 90% chord. Following Bendat and Piersol [45] and assuming a 0.9 coherence, the normalized random errors for the autospectrum, cross-spectrum, coherence, coherent output power, and transfer function were 0.250, 0.264, 0.037, 0.276, and 0.0589, respectively.

The fin constraint forces/moments were measured with a custom four-component load cell (Fig. 2). The center shaft had four 7.62 mm square pockets (P1 and P2 in Fig. 2) to form two thin membranes (rotated 90 deg relative to each other) for lift and drag measurements. A center hole created a 0.71 mm thin-walled section to facilitate torque and drag-moment measurements. Each cell had a Wheatstone bridge of strain gauges (lift, drag, torque: sk-06-062TW-350, Vishay; y -moment: TK-06-092P-10C/DP, Vishay). Bridges were excited with 10 volts direct current (VDC) and the output sampled at 1 kHz. The load cell measured lift force ($\mathcal{L}$), drag force ($\mathcal{D}$), y-axis moment (drag-moment; M_D), and the z-axis moment (torque; T_q) when at $\alpha = 0$ deg, which were corrected for $\alpha = -9.6$ deg. A benchtop calibration matrix was formed from 356 samples using a range of loads, locations, and fin orientations, which was confirmed with an in situ calibration. The random and bias errors were quantified from the mean residual loads, which are in Table 3. Given the nominal test range, the uncertainty of the lift and drag-moment were about 5%, while the drag and torque were 7–10%.

Water temperature (resistance temperature detector sensor; 911PL, Stow Laboratories), total tunnel pressure (Kiel probe), local static pressure, and tunnel impeller frequency (f_{imp}) were recorded at 1 kHz. Static pressure ports were located at $x = 0$, 75, 175, 280, 385, and 490 mm as well as by the Kiel probe. The local freestream speed was determined from the difference between total and static pressure, which was confirmed with PIV and LDV.

2.4 Test Conditions. This study focuses on the fin in the rough cylinder wake, but three other configurations were tested: (i) empty test section, (ii) smooth cylinder only, and (iii) rough cylinder only. These results as well as additional setup details are in Elbing et al. [44], and some of these results are included here to assist in interpretation and provide model validation data. During forced fin testing, f_{imp} varied between 50 and 84 rpm and α was −9.6 deg. The average water temperature was 20.5 ± 0.5 °C, which sets the water density (ρ) and kinematic viscosity (ν) at 998 kg/m^3 and 9.9×10^{-7} m^2/s, respectively.

3 Flow Inlet Characterization

A direct measure of the inlet velocity was not possible due to the close proximity of the cylinder. Thus, the volumetric flowrate was determined from integration of the velocity across the test section

Table 3 Mean residual loads as a percentage of full scale (f.s.) from the load cell calibration and the resulting uncertainty range

Component	Mean residual	f.s.	Uncertainty
Lift force ($\mathcal{L}$)	±0.3% f.s.	110 N	±0.3 N
Drag force (D)	±2.0% f.s.	20 N	±0.4 N
Torque (Tq)	±1.0% f.s.	5.4 N·m	±0.05 N·m
Drag-moment (M_D)	±0.5% f.s.	4.7 N·m	±.02 N·m

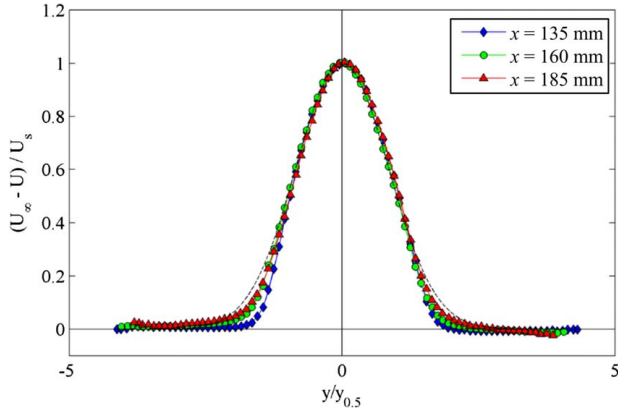

Fig. 4 Normalized average wake velocity deficit profiles. Dashed line is a self-similar plane wake solution [46].

cross-sectional area since detailed surveys of the wake, freestream, vertical variation, and wall boundary layers were performed. The mean wake velocity profiles in Fig. 4 scale like a self-similar plane wake [46], where U is the local mean streamwise velocity, $U_S(=U_\infty - U(x, y = 0))$ is the velocity deficit, and $y_{0.5}$ is the wake half-width defined as $U(x, \pm y_{0.5}) = U_\infty - 0.5U_S(x)$. The current results approach a self-similar constant turbulent viscosity plane wake, $(U_\infty - U)/U_S = \exp(-0.693(y/y_{0.5}(x))^2)$, with increasing downstream distance. Table 4 provides the average velocity at the test section inlet (U_{in}) at each f_{imp}, which is the volumetric flowrate divided by the inlet area. Table 4 also includes the wake scaling parameters, U_{sp} the average freestream speed spanning the fin location ($x = 175$–490 mm), U_C the centerline ($y = 0$) streamwise velocity one chord length upstream of the fin tip ($x = 185$ mm), and U_∞ a PIV freestream speed measurement. The freestream speeds from PIV and static pressure were within ~2%. The forced fin analysis primarily uses U_{sp} since it is the freestream at the fin.

4 Cylinder Characterization

4.1 Base Pressure. The flow around the three cylinder configurations (smooth, rough, and rough with fin) were characterized with the base static and dynamic pressures. The base pressure coefficient ($C_{pb} = \Delta P_b / 0.5\rho U_\infty^2$) is commonly used to characterize cylinder flow because it is directly related to the drag, where ΔP_b is the difference between base ($\theta = 180$ deg) and local static pressures. Figure 5 provides C_{pb} versus $\text{Re}_D(=U_\infty D/\nu)$ at the fin mid-span ($z = 115$ mm) and tip ($z = 230$ mm) heights for all three configurations. For reference, a representative smooth cylinder curve [47]

Table 4 Average speeds (including the mean inlet velocity) at each f_{imp} and wake velocity deficit scaling parameters

f_{imp} (Hz)	U_{in} (m/s)	U_{sp} (m/s)	U_C (m/s)	x (mm)	U_∞ (m/s)	U_S (m/s)	$y_{0.5}$ (mm)
58.3	2.10	2.51	1.19	135	2.59	2.51	21.1
				160	2.48	1.79	22.2
				185	2.42	1.25	25.8
69.6	2.57	2.99	1.13	135	3.21	3.29	22.7
				160	3.09	2.56	22.3
				185	3.00	1.89	23.4
80.1	2.87	3.44	1.11	135	3.66	3.91	23.9
				160	3.48	3.10	22.3
				185	3.36	2.27	22.3
84.2	3.17	3.62	1.57	135	3.89	3.80	23.2
				160	3.77	2.89	23.6
				185	3.69	2.13	25.1

Downloaded from http://asmedigitalcollection.asme.org/vibrationacoustics/article-pdf/142/4/041014/6527766/vib_142_4_041014.pdf by guest on 23 April 2024

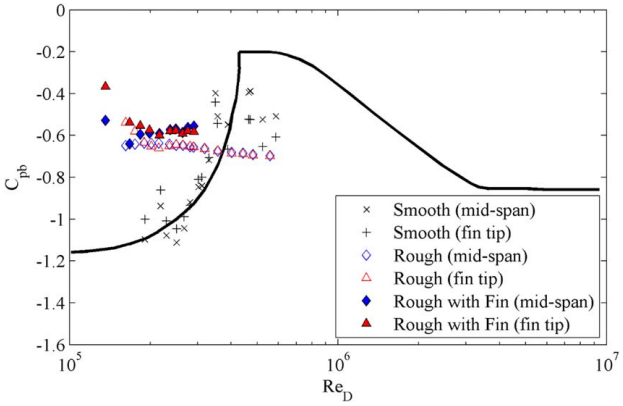

Fig. 5 Base pressure coefficient versus Reynolds number with a representative smooth cylinder curve [47] for reference

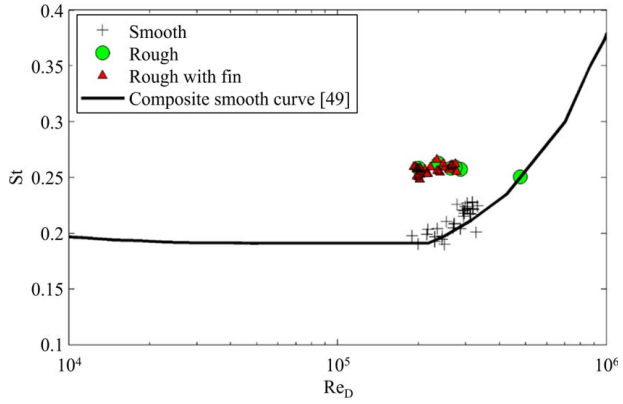

Fig. 7 Strouhal scaling of the shedding frequency versus Reynolds number compared with a representative composite smooth cylinder curve [49]

is included. The smooth results follow the reference curve with scatter that is consistent with historical data [40,47,48]. This shows that the smooth cylinder was in the transitional range, which motivated roughening the leading edge. The rough results closely follow the data used to size and position the roughness [40], which has a weak Re_D dependence. Minimal spanwise variation is observed with and without the fin installed, but there is a measurable shift in the cylinder performance with the fin installed. This shift was likely due to the oscillating fin impacting the free-stream speed measurement, not the actual cylinder flow field. Regardless, it is apparent that with the fin installed there was minimal spanwise variation and over the operation range the behavior is nearly independent of Re_D.

4.2 Shedding Frequency. Spectral analysis of the dynamic pressure on the aft side of the cylinder was used to identify the vortex shedding frequency. The smooth cylinder showed increasing shedding frequency and root-mean-squared (RMS) levels with increasing speed until ~3 m/s ($Re_D = 1.8 \times 10^5$). At higher speeds, the peak weakens and eventually disappears ($Re_D = 2.4 \times 10^5$) due to the laminar-to-turbulent transition of the boundary layer, which makes the wake incoherent. The rough cylinder has increasing frequency and RMS levels up to the max speed of 6 m/s ($Re_D = 3.6 \times 10^5$), but it also had three additional spectral peaks. For example, the power spectra (Φ_{dp}) at $U_{sp} = 2.99$ m/s are shown in Fig. 6 and

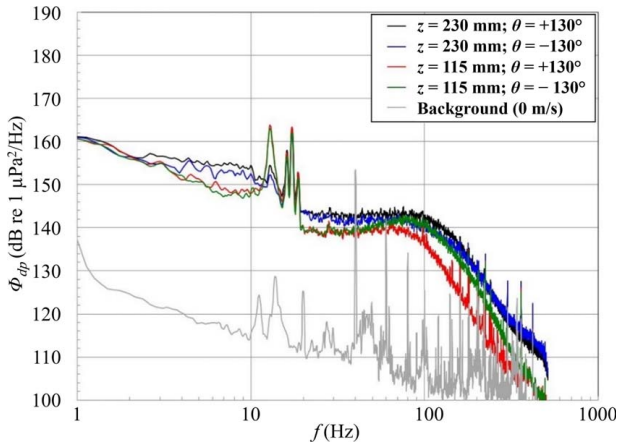

Fig. 6 Rough cylinder pressure spectra at $U_{sp} = 2.99$ m/s. Also included is the electrical background spectrum (0 m/s) from one sensor.

spectral peaks are observed at 13 (shedding frequency), 16, 17.1, and 18.6 Hz. Estimating the fluctuating lift and drag forces on the cylinder showed that the three higher frequency peaks are only in the drag force spectra. Since LDV confirmed that the tunnel speed was stable and repeatable, the most likely cause for these extra peaks in the drag spectra were either noise contamination or spanwise variations. Fortunately, the fin loading was primarily dependent on the lift, which did not have these extra peaks, but it does have the 13 Hz shedding frequency. The spanwise coherence at the shedding frequency was high on both sides of the cylinder. Comparison of rough cylinder spectra with and without the fin shows that there was no significant variation in peak RMS levels at the shedding frequency, in spite of the slight variation in C_{pb}. This finding supports the previous conjecture that the C_{pb} variation was due to the fin's influence on the velocity measurement and not an alteration to the flow field.

Figure 7 shows the Strouhal number ($St = f_s D/U_\infty$) versus Re_D for all configurations, where f_s is the cylinder vortex shedding frequency. The current smooth data are in agreement with a composite curve for smooth cylinders [49], though no shedding was observed for $Re_D \geq 3.3 \times 10^5$. Conversely, the rough cylinders had a nearly constant St (0.26) over the range of Re_D tested, which is slightly lower than that reported in the literature [40] over the same Re_D range. Bias error was quantified by comparing independent measurements (dynamic pressure, accelerometer, and LDV), and the random error was determined from comparisons between repeated test conditions. The bias and random errors were ±1.2% and ±2% with a 95% confidence, which sets the accuracy of f_s at ±2.3%.

5 Forced Fin Results

5.1 Flow Field (Cylinder Wake). The streamwise (u) and cross-stream (v) velocities were measured upstream of the fin at 82% span ($z = 188$ mm). Figure 8 provides the average streamwise (U), fluctuating streamwise (u'), average cross-stream (V), and fluctuating cross-stream (v') velocity profiles scaled with U_{sp} and plotted versus the y-coordinate scaled with D at three streamwise locations ($x/D = 2.25$, 2.67, 3.08). The upstream cylinder blockage causes the mean streamwise velocity outside of the wake to exceed U_{sp} in the near-wake region, with this effect decreasing with increasing downstream distance. The mean and fluctuating streamwise velocity profiles show the wake width spreading and wake deficit decreasing with increasing downstream distance. The u' profiles have a bimodal distribution with peaks at nominally $\pm 0.4D$, which also decreases with increasing downstream distance. The asymmetry of the peaks is likely due to the fin oscillations causing a periodic blockage downstream, which was biased toward the negative y side due to the angle-of-attack. However,

Downloaded from http://asmedigitalcollection.asme.org/vibrationacoustics/article-pdf/142/4/041014/6527766/vib_142_4_041014.pdf by guest on 23 April 2024

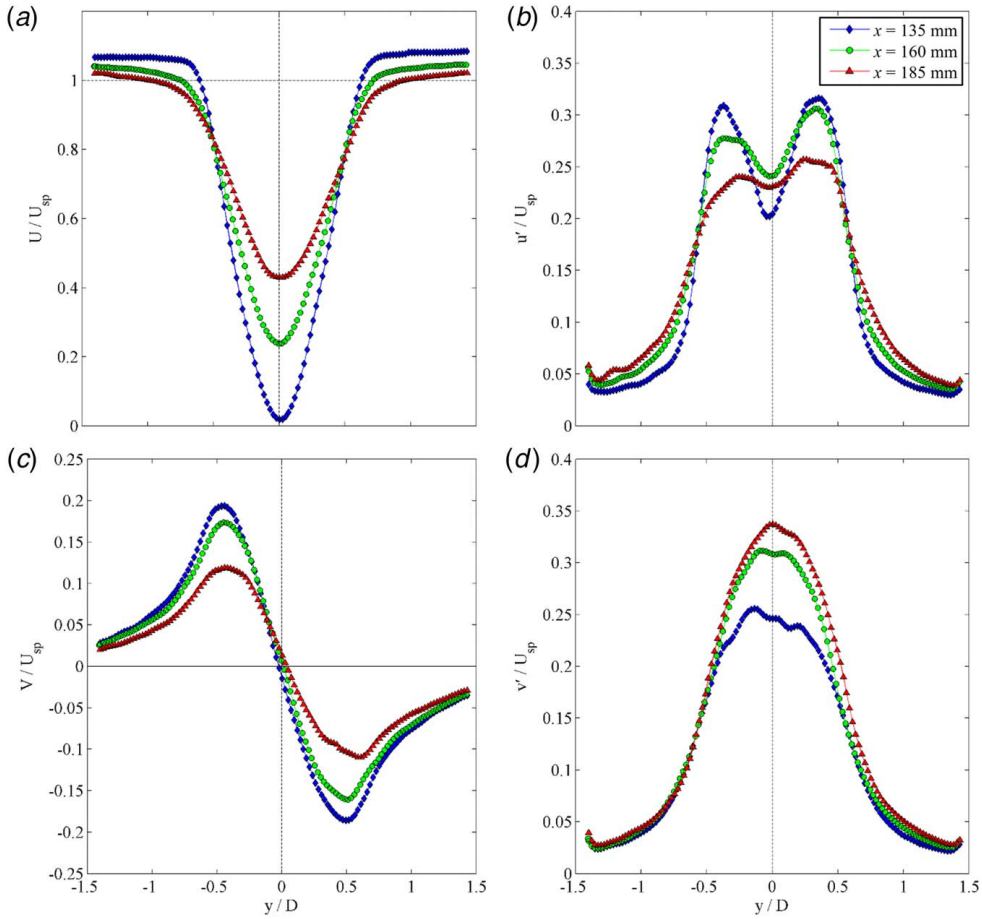

Fig. 8 The scaled ($U_{sp} = 3.62$ m/s) mean (*a*, *c*) and fluctuating (*b*, *d*) velocity profiles versus *y/D*. The top (*a*, *b*) and bottom (*c*, *d*) rows are the streamwise and cross-stream components, respectively.

due to the spreading wake, the fluctuating velocity increases with increasing downstream distance for $|y/D| > 0.6$. The V profiles are approximately zero at the centerline and symmetric in magnitude about the centerline with peaks near $y/D = \pm 0.5$. Since these positions are beyond the recirculation region ($x/D \sim 2.2$), the peaks decrease with increasing downstream distance. The centerline v' increases with increasing downstream distance, but this trend ceases beyond $x = 185$ mm (data not shown since the goal is to characterize the cylinder wake upstream of the fin).

The spatial distribution of the fluctuating velocity was examined via spatial correlations and wavenumber spectra. The spatial autocorrelation for a homogeneous velocity component u is defined as $R_{uu}(\xi,\ \eta) = E[u(x,\ y)u(x+\xi,\ y+\eta)]$, where $E[-]$ is the expected value and ξ and η are relative distances in the x and y directions, respectively. The spatial autocorrelation is even (symmetric), thus all spatial autocorrelations are shown for positive separation distances only. Contour plots of the spatial autocorrelation distribution for u and v are in Elbing et al. [44] with a general shape similar between speeds and the peak correlations increasing with velocity. The autocorrelation for u and v with streamwise (Δx) and cross-stream (Δy) separation distances is shown in Fig. 9. The autocorrelations are normalized by the variance (σ_u^2 or σ_v^2), which was 0.02 m^2/s^2 for the v and u was 0.16, 0.2, and 0.35 m^2/s^2 for $U_{sp} =$ 2.51, 2.99, and 3.62 m/s, respectively. The streamwise variance was proportional to tunnel speed squared, and all the profiles have similar trends for a given speed and direction. The minimum at approximately 70 mm followed by a local maximum at approximately 140 mm in the streamwise direction (x) corresponds to the half wavelength (i.e., out-of-phase) and full wavelength of the shed vortices.

The wavenumber (k) spectrum is the Fourier transform of the autocorrelation in both x and y directions

$$S_{uu}(k_x,\ k_y) = \int_{-\infty}^{\infty}\int_{-\infty}^{\infty} R_{uu}(\xi,\ \eta)\exp[-i(k_x\xi + k_y\eta)]d\xi d\eta$$

Since the spatial autocorrelation is even along both axes, the corresponding autospectrum is real and even (symmetric). Thus, only the positive wavenumbers (k_x, k_y) are shown. These wavenumber spectra were computed using the indirect fast Fourier transform (FFT) approach [50]. The range was extended by padding the velocity with zeroes and a Hanning window was applied to the spatial data. The FFT of the extended velocity data was used to estimate the autospectral density, and then the inverse FFT of the autospectral density gives the autocorrelation. Assuming a coherence of 1.00, the normalized random error for the autospectrum was 0.154 or 0.6 dB. Contour plots of the spatial distribution of S_{uu} and S_{vv} are in Elbing et al. [44], and Fig. 10 shows autospectra curves extracted from the contour plots versus k_x for various constant k_y values. Comparison of these wavenumber spectra with those acquired without the fin installed (not shown) show negligible variation, which shows that there were no feedback mechanisms between the upstream flow-field and the fin at this location.

5.2 Fin Motion. High-speed imaging measured the maximum deflections (translational motion) and twist (rotation) at the fin tip. The fin tip twist (ϕ_t) results reveal a linear relationship with the tunnel speed, $\phi_t = 0.20U_{sp} - 0.372$, between $2.5 \le U_{sp} \le 3.4$. In general, there was minimal twist with the maximum mean and RMS twist being 0.31 deg and 0.33 deg, respectively. Fin tip

Downloaded from http://asmedigitalcollection.asme.org/vibrationacoustics/article-pdf/142/4/041014/6527766/vib_142_4_041014.pdf by guest on 23 April 2024

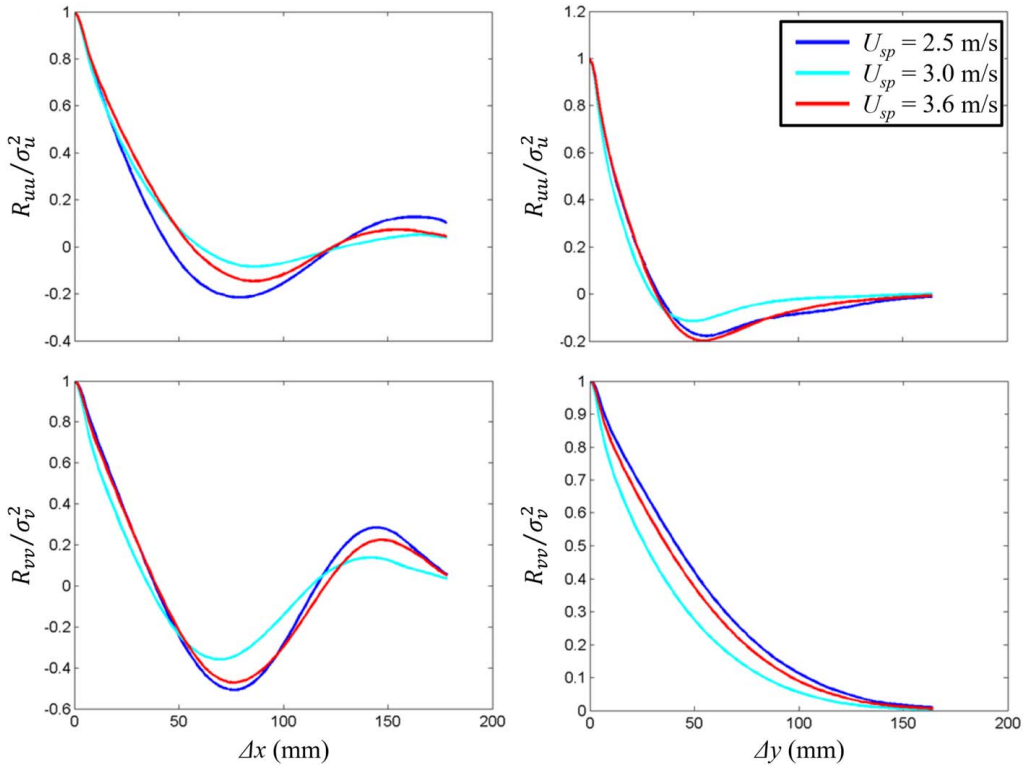

Fig. 9 Comparison of the spatial autocorrelations along the *x*- and *y*-axis for the *x*- and *y*-velocity components

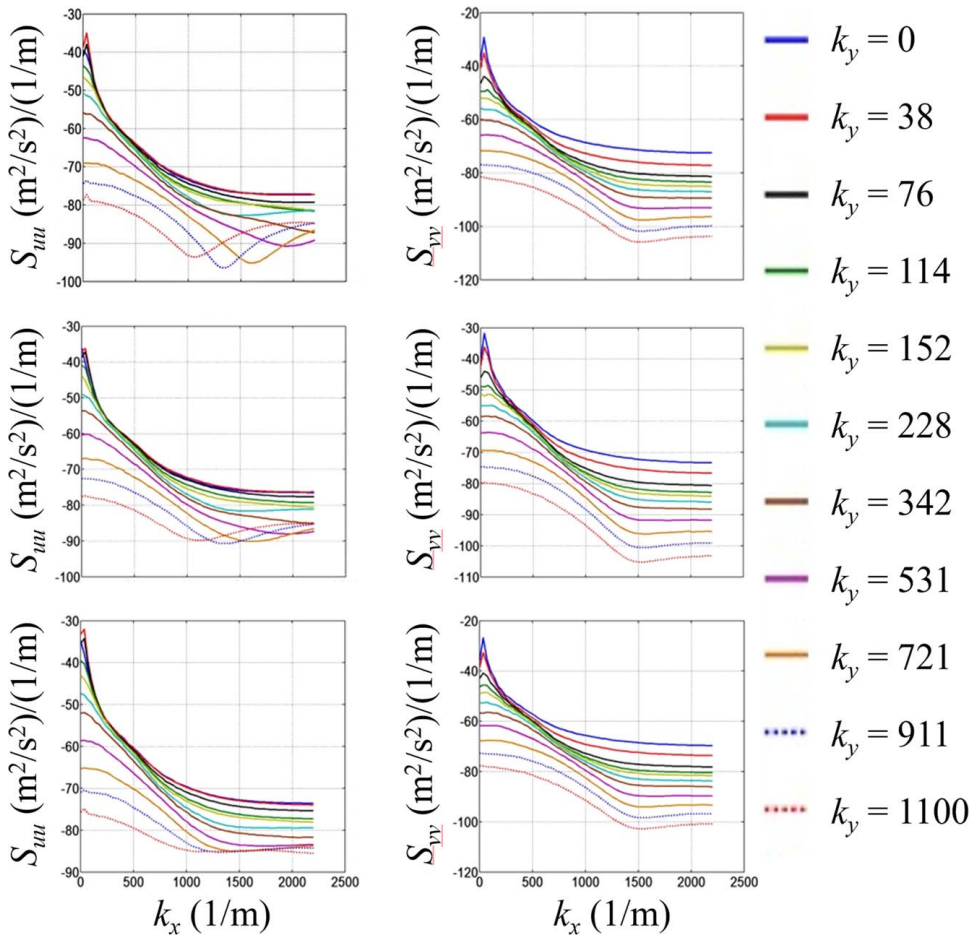

Fig. 10 Wavenumber spectra for the (left) *x*- and (right) *y*-velocity components at U_{sp} = (top) 2.52, (middle) 2.99, and (bottom) 3.62 m/s. The bandwidth along k_x is 35.1 m^{-1}.

Downloaded from http://asmedigitalcollection.asme.org/vibrationacoustics/article-pdf/142/4/041014/6527766/vib_142_4_041014.pdf by guest on 23 April 2024

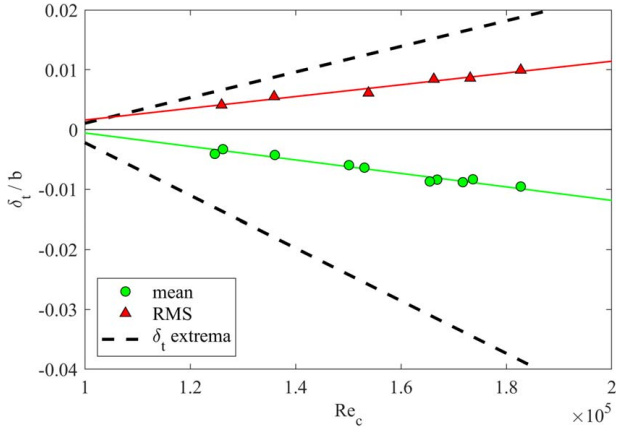

Fig. 11 Fin tip deflections (mean and RMS) scaled with the fin span (230 mm) versus Reynolds number. Dashed and solid lines are the nominal extrema and linear best fits (mean or RMS) of the deflections, respectively.

deflection mean (δ_t) and RMS (δ_t') values scaled by the fin span ($b=230$ mm) as a function of the chord ($c=49.5$ mm) based Reynolds number ($\mathrm{Re}_c = U_{sp}c/\nu$) are in Fig. 11. The mean and RMS fin tip deflections were linearly fitted resulting in $\delta_t/b = -1.13\times10^{-7}\,\mathrm{Re}_c + 0.011$ and $\delta_t'/b = 9.85\times10^{-8}\mathrm{Re}_c - 0.0083$, respectively. Note that a power-law fit was equally valid, but with a narrow Re_c range the power could not be accurately estimated. Also in Fig. 11 are dashed lines marking the nominal range of the fin tip deflection extrema, which were approximately ±2.9 times δ_t. The mean deflection became more negative with increasing speed due to the negative angle-of-attack. The uncertainty in the mean and RMS tip deflections are ±7% (≤±0.15 mm) and ±9% (≤±0.2 mm) of the measurement, respectively. This uncertainty was primarily due to the combination of a relatively short sample period (3 s) and broadband frequency content.

While the broadband frequency was apparent in the fin tip displacement time traces, spectral analysis was not performed due to the limited period. However, the peak in the autocorrelation was at f_s. Consequently, spectral density of the fin motion was examined with the surface laser vibrometer. A typical deflection RMS amplitude spectrum Φ_δ (square root of the autospectrum level) from a single point (90% span, 50% chord) is shown in Fig. 12. Two peaks were observed below 50 Hz, with the first and second corresponding to f_s and first fin bending mode, respectively. The peak at about 100 Hz corresponds to the in-water second cross-stream bending mode with no apparent peak at the first streamwise

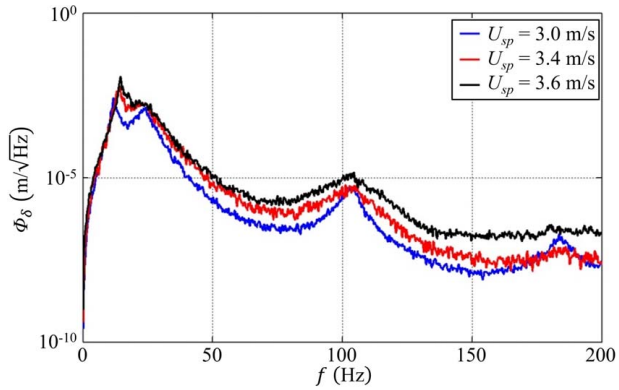

Fig. 12 Fin deflection RMS spectra near the fin tip (90% span) at 50% chord

bending mode (~44 Hz). This is consistent since surface vibrometers only measure the normal surface motion (i.e., more sensitive to cross-stream motion than streamwise in the current setup). As expected given the deflection spectrum, the predominant mode near the shedding frequency is the first bending mode with the largest deflections occurring near the fin tip (see Ref. [44]; for example, contour plots). The surface deflection results are provided in Table 5, including the peak frequency (f_{pk}), the corresponding RMS level, and the quality factor. The quality factor ($Q = f_{pk}/(f_U - f_L)$) is a measure of the bandwidth of the peak, where f_U and f_L are the frequency 3 dB below the peak on the upper and lower side of the peak, respectively. In addition, the average and standard deviation of f_{pk} and Q are provided. These results show that f_{pk} increases with speed but remains relatively stable independent of speed. The width of the peak broadens (i.e., Q increases) with increasing speed and experiences larger fluctuations.

Since the fin was excited by coherent structures, it is of interest to examine the coherence of these fin surface motions. The coherence can be quantified as

$$\gamma_{xy}^2 = \frac{|G_{xy}(f)|^2}{G_{xx}(f)G_{yy}(f)}$$

where G is either the cross-spectrum (G_{xy}) or autospectrum (G_{xx},G_{yy}) at a given frequency (f) between given points (x,y) on the fin surface [45]. Figure 13 shows the coherence as a function of separation distance between each location and the reference point (80% span, 90% chord). As expected, the coherence decreases with increasing separation distance and frequency. The shedding frequency at this speed ($U_{sp}=3.62$ m/s) was 14.5 Hz, which has high coherence over nearly the entire range. The high coherence reflects the fact that the fin vibration is dominated by a single mode.

5.3 Fin Constraint Forces and Moments. The load cell measured the constraint lift ($\mathcal{L}$), drag ($\mathcal{D}$), torque (T_q), and drag-moment (M_D), which is the constraint moment about the axis perpendicular to the chord length. Time traces show that f_s dominates the oscillations with additional broadband content, and $\mathcal{L}$ is 180 deg out-of-phase with the other constraint forces/moments [44]. The mean coefficient of lift ($C_L \equiv \mathcal{L}/(0.5\rho U_{sp}^2 bc)$), drag ($C_D \equiv \mathcal{D}/(0.5\rho U_{sp}^2 bc)$), drag-moment ($C_{MD} \equiv M_D/(0.5\rho U_{sp}^2 b^2 c)$), and torque ($C_{Tq} \equiv T_q/(0.5\rho U_{sp}^2 b^2 c)$) were all independent of Reynolds number over the narrow test range (10^5 to 1.8×10^5). The average values were -0.200 ± 0.018, 0.114 ± 0.007, 0.040 ± 0.002, and 0.0287 ± 0.002 for C_L, C_D, C_{MD}, and C_{Tq}, respectively. Here, the uncertainties are twice the standard deviation from measurements at different Reynolds numbers. Note that the mean negative $\mathcal{L}$ is consistent with non-zero mean fin tip deflections at a given speed. Torque and drag-moment data enable the calculation of the center of pressure in two directions. Torque on the fin was induced by the lift and drag forces, suggesting that the resultant load acts at a distance R_T from the center of the load cell. This distance was determined by dividing the torque by the magnitude of the lift and drag forces and should be a constant because the constraint force coefficients and the span were constant. The resultant torque moment arm was $R_T = 29.2\pm2.0$ mm, with the uncertainty being twice the standard deviation from results at each speed. This shows that the center of pressure was located more than half a chord length from the load cell center due to the forward sweep of the fin. In addition, the drag-moment was used to determine the spanwise location of the center of pressure. Since the load cell was zeroed before testing, the weight was assumed negligible, and thus, the force parallel to the chord was the only loading considered. The spanwise center of pressure was at $z = 119\pm14$ mm with the uncertainty being twice the standard deviation at each speed. The center of pressure was slightly above the center of the span and experienced larger variations than the torque moment arm.

The RMS constraint forces/moments were scaled with their respective mean values and plotted versus the chord-based

Downloaded from http://asmedigitalcollection.asme.org/vibrationacoustics/article-pdf/142/4/041014/6527766/vib_142_4_041014.pdf by guest on 23 April 2024

Table 5 Fin surface deflection peak frequency (f_{pk}), peak RMS level, and peak quality factor (Q)

		$U_{sp}=2.99$ m/s			$U_{sp}=3.44$ m/s			$U_{sp}=3.62$ m/s		
Span (%)	Chord (%)	f_{pk} (Hz)	Peak (RMS m/s)	Q (–)	f_{pk} (Hz)	Peak (RMS m/s)	Q (–)	f_{pk} (Hz)	Peak (RMS m/s)	Q (–)
40	90	12.0	0.44	10.7	13.9	1.49	12.3	14.5	2.49	19.3
40	50	11.9	0.41	9.5	14.0	1.01	10.2	14.5	2.25	14.5
40	10	11.5	0.32	11.5	13.5	0.91	9.0	14.0	1.55	8.0
50	90	11.9	0.58	7.3	14.3	1.95	11.4	14.4	2.22	9.6
50	50	11.6	0.42	6.2	13.8	2.70	11.0	14.5	3.98	14.5
50	10	11.9	0.63	9.5	13.5	1.77	8.3	14.5	2.51	8.9
60	90	12.1	0.96	6.9	13.8	3.92	15.7	14.3	4.04	6.0
60	50	11.9	1.10	13.6	13.6	2.99	9.9	14.1	3.25	8.7
60	10	12.0	0.72	7.4	13.6	3.16	9.9	14.4	3.86	9.6
70	90	11.9	1.26	9.5	13.8	5.48	11.0	14.3	6.01	14.3
70	50	11.9	1.25	7.9	13.8	2.94	4.6	14.0	4.17	8.0
70	10	12.4	1.62	9.0	14.0	5.11	10.2	14.8	5.34	14.8
80	90	11.6	1.51	4.7	13.8	4.34	6.1	14.8	8.18	16.9
80	50	12.3	1.41	6.5	14.1	5.82	9.4	14.3	7.14	10.4
80	10	12.1	1.57	6.9	14.0	4.27	9.3	14.4	8.07	8.9
90	90	11.6	2.25	8.5	13.6	6.63	8.4	14.8	10.6	13.1
90	50	11.6	2.29	6.6	14.0	5.60	11.2	14.6	10.6	9.8
90	10	11.8	2.22	5.5	13.5	5.15	6.0	14.4	11.2	11.5
95	90	11.8	2.61	9.4	13.5	6.61	7.7	14.5	11.5	11.6
95	50	12.0	2.56	8.0	13.3	5.35	5.6	14.6	11.4	11.7
95	10	11.6	2.10	6.2	14.0	4.45	5.1	14.6	12.6	10.6
	Average	11.9		8.2	13.8		9.2	14.4		11.5
	Standard deviation	0.2		2.1	0.3		2.7	0.2		3.3

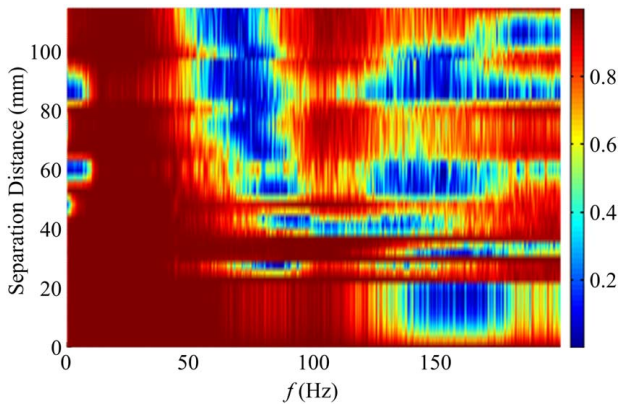

Fig. 13 Contour plot of the fin motion coherence versus frequency and separation distance relative to 80% span and 90% chord ($U_{sp}=3.62$ m/s)

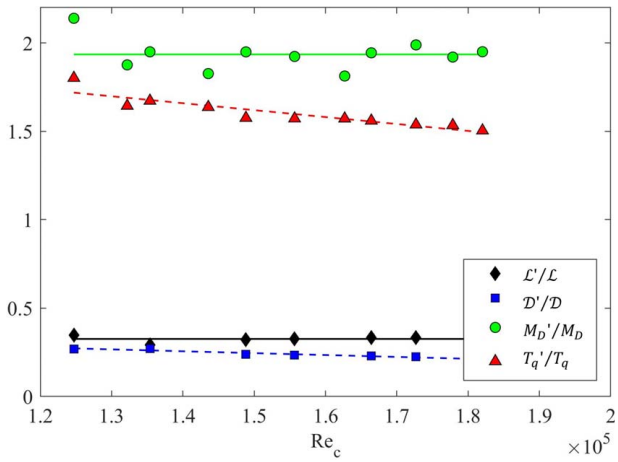

Fig. 14 RMS constraint forces/moments scaled with their mean values versus Reynolds number. Solid lines are average values, and dashed lines are linear fits.

Reynolds number (Re_c) in Fig. 14. Linear regression analysis of these curves shows that the slope of the fluctuating drag and torque is statistically significant (p-value < 0.05). The resulting linear fits for the fluctuating drag and torque curves are $\mathcal{D}'/|\mathcal{D}| = -1.07\times10^{-6}\mathrm{Re}_c + 0.405$ and $T_q'/|T_q| = -3.92\times10^{-6}\mathrm{Re}_c + 2.21$, respectively. Conversely, the fluctuating lift and drag-moment curves were independent of Re_c with $\mathcal{L}'/|\mathcal{L}| = 0.326 \pm 0.038$ and $M_D'/|M_D| = 1.935 \pm 0.174$, where the uncertainty is twice the standard deviation. In general, these data are more scattered than the mean due to the broadband nature of the cylinder vortex shedding coupled with the structural response of the fin. Consequently, it is more informative to investigate the spectral content.

The power spectral density of $\mathcal{L}$ was examined to assess the repeatability and sensitivity to angle-of-attack. Figure 15(*a*) shows repeated (seven total) measurements of the power spectral density of the fin constraint lift force ($\Phi_{\mathcal{L}}$) at $\alpha = -0.8$ deg and $U_{sp} = 3.1$ m/s. These results consistently show a peak RMS lift force at the shedding frequency of 16.66 ± 0.38 N, or approximately $\pm 2.3\%$ uncertainty. The peak (shedding) frequency varied by $\pm 1.5\%$ at 13.67 ± 0.02 Hz. Figure 15(*b*) compares the sensitivity of the lift power spectral density to angle-of-attack at the same speed ($U_{sp} = 3.1$ m/s). The angle-of-attack has minimal impact on the fluctuating fin lift forces at the shedding frequency, with the peak RMS lift force (16.69 ± 0.43 N) within the uncertainty range of the repeated -0.8 deg condition. While this implies that the angle-of-attack does not impact the fluctuating lift force, the angle-of-attack does impact the mean lift force. Note that due to concerns of overstraining the load cell and/or exceeding the designed fin deflections, a mechanical stop that bracketed the fin tip was installed for these initial measurements. Figure 15(*b*) includes a repeated condition with the mechanical stop removed that shows the stop had negligible impact on the fin loading. Overall these results provide confidence in the repeatability of the facility and the fluid loading.

Figure 16(*a*) shows the power spectral density of the constraint forces/moments at $U_{sp} = 3.44$ m/s and $\alpha = -9.6$ deg. These data

Downloaded from http://asmedigitalcollection.asme.org/vibrationacoustics/article-pdf/142/4/041014/6527766/vib_142_4_041014.pdf by guest on 23 April 2024

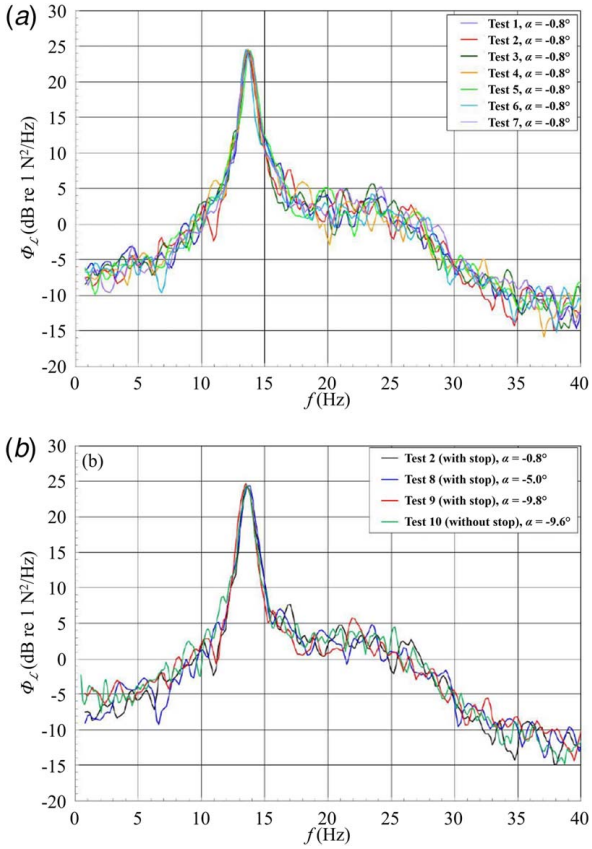

Fig. 15 Power spectral density of the lift force at $U_{sp} = 3.1$ m/s for (*a*) a repeated condition and (*b*) varying α

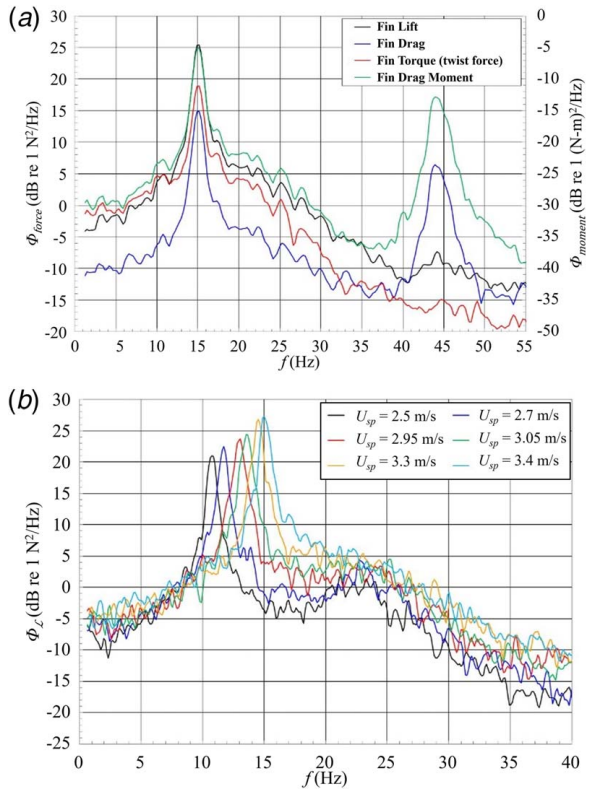

Fig. 16 Power spectral densities for (*a*) the constraint forces/moments ($U_{sp} = 3.44$ m/s) and (*b*) the lift force at various speeds

show that the fin lift force at the shedding frequency of 14.9 Hz was approximately 10 dB greater than the drag component. The drag force and drag-moment have an additional peak at ~44 Hz, which was not observed in the torque or lift force. This is due to the first streamwise bending mode (Table 2), since modes in the streamwise direction would only be observed in the loading associated with the drag. The first cross-stream bending mode (23 Hz) was not apparent in these data, but a slight plateau in the spectral levels coming down from the shedding frequency appears to hold until ~23 Hz before decreasing more rapidly. At the shedding frequency, the RMS fin torque (twist) was 0.275 N·m (−11.2 dB), which is nearly an order of magnitude less than the moment applied during the static load testing. This result is consistent with the RMS fin tip twist measurements that showed only a few tenths of a degree of movement.

The speed dependence was also examined with Fig. 16(*b*) showing $\Phi_{\mathcal{L}}$ spanning the range of test speeds. It is apparent that the peak frequency and amplitude increase with increasing speed. Note that the lowest speeds appear to have a weak secondary peak between 20 and 25 Hz that corresponds to the first cross-stream bending mode (Table 2). The peak frequencies match the cylinder shedding frequency with a constant $\mathrm{St} = 0.263 \pm 0.007$, where the uncertainty is twice the standard deviation. The peak amplitudes were 11.2, 13.4, 15.3, 16.7, 21.7, and 23.1 N for $U_{sp} = 2.5$, 2.7, 2.95, 3.05, 3.3, and 3.4 m/s, respectively. These amplitudes are well approximated as a power-law function with the amplitude being proportional to $U_{sp}^{2.6}$.

6 Summary and Conclusions

A turbulent high-amplitude, low-frequency flow-induced FSI experiment was performed with a backward-facing, 49.5 mm chord swept-fin mounted on a load cell and located in the wake of 60 mm diameter cylinder to mimic crashback [17]. The fin angle-of-attack was fixed at −9.6 deg since the fluctuating loading was insensitive to angle-of-attack. The geometry (tunnel, cylinder, fin, and load cell), fluid properties, and material properties/response are provided in Sec. 2. The flow-field and fin response are characterized with wake flow-field measurements (PIV and LDV), fin motion (high-speed imaging and surface laser vibrometer), and constraint forces/moments (lift, drag, torque, and drag-moment).

Tip deflections increased linearly with Re_c with the peak-to-peak fin tip deflections being 5.8 times the mean deflections. The corresponding mean constraint force/moment coefficients were constant. The center of pressure for the resultant load is located at $z = 119$ mm with a torque moment arm of 29.2 mm from the center of the load cell. Wavenumber spectral analysis of the cylinder fluctuating wake profiles shows that there was no feedback mechanism between the fin and the upstream cylinder wake. The fluctuating lift force and drag-moment are constant, but the drag force and torque are proportional to Re_c. The fin surface deflections show distinct peaks at the cylinder shedding frequency ($\mathrm{St} = 0.26$), the first cross-stream bending mode (23 Hz) and the second cross-stream bending mode (103 Hz). The constraint force/moment spectra capture the first two peaks, and the first streamwise bending mode (44 Hz) was also observed in the drag related spectra. The constraint force/moment amplitudes at the shedding frequency were proportional to $U_{sp}^{2.6}$.

This paper provides a challenging real-world benchmark problem for FSI validation due to the large fin oscillations induced by a complex turbulent flow-field. Presented is the information required to setup the initial conditions for modelers as well as several independent measurements characterizing the response of the forced fin. This rich dataset may be used for FSI validation. Further, it will give modelers the ability to identify strengths and weaknesses of various modeling approaches for solving such complex FSI problems. This will become more important as composite materials are explored for propulsion schemes, especially for marine applications.

Downloaded from http://asmedigitalcollection.asme.org/vibrationacoustics/article-pdf/142/4/041014/6527766/vib_142_4_041014.pdf by guest on 23 April 2024

Acknowledgment

The authors would like to thank the technical staff at the ARL, especially Mr. Neil Kimerer for the load cell design and Dr. Arnie Fontaine with the experimental design. We would also like to thank Drs. Peter Chang and Scott Black for guidance throughout the experiment.

Funding Data

- This research was sponsored by DARPA under Contract No. N0002402-D-6604 (Dr. Christopher Warren, Program Manager). This document does not necessarily reflect the position or policy of the U.S. Government, and no official endorsement should be inferred.

References

[1] Bridges, D. H., 2004, "A Detailed Study of the Flow Field of a Submarine Propeller During a Crashback Maneuver," Mississippi State University, Technical Report MSSU-ASE-04-1.
[2] Jessup, S., Fry, D., and Donnelly, M., 2006, "Unsteady Propeller Performance in Crashback Conditions With and Without a Duct," Proceedings of the 26th Symposium on Naval Hydrodynamics, Rome, Italy, Sept. 17–22.
[3] Vyšohlíd, M., and Mahesh, K., 2006, "Large Eddy Simulation of Crashback in Marine Propellers," Proceedings of the 26th Symposium on Naval Hydrodynamics, Vol. 9, Rome, Italy, Sept. 17–22, pp. 237–262.
[4] Chang, P. A., Ebert, M. P., Shipman, J., and Mahesh, K., 2008, "Prediction of High-Amplitude Forces During Propeller Crashback," DoD HPCMP Users Group Conference, IEEE Xplore, Seattle, WA, July 14–17, p. 10401472.
[5] Bridges, D. H., Donnelly, M. J., and Park, J. T., 2008, "Experimental Investigation of the Submarine Crashback Maneuver," J. Fluid. Eng., **130**(1), p. 0111031.
[6] Davoudzadeh, F., Taylor, L. K., Zierke, W. C., Dreyer, J. J., McDonald, H., and Whitfield, D. L., 1997, "Coupled Navier-Stokes and Equations of Motion Simulation of Submarine Maneuvers, Including Crashback," 1997 ASME Fluids Engineering Division Summer Meeting, Vancouver, Canada, June 22–26, FEDSM97, Part 16.
[7] Chen, B., and Stern, F., 1999, "Computational Fluid Dynamics of Four-Quadrant Marine-Propulsor Flow," J. Ship Res., **43**(4), pp. 218–228.
[8] Verma, A., Jang, H., and Mahesh, K., 2012, "The Effect of an Upstream Hull on a Propeller in Reverse Rotation," J. Fluid Mech., **704**, pp. 61–88.
[9] Jang, H., Verma, A., and Mahesh, K., 2012, "Predicting Unsteady Loads in Marine Propulsor Crashback Using Large Edge Simulation," Int. J. Rotating Mach., **2012**, pp. 1–12.
[10] Mouritz, A. P., Gellert, E., Burchill, P., and Challis, K., 2001, "Review of Advanced Composite Structures for Naval Ships and Submarines," Compos. Struct., **53**(1), pp. 21–24.
[11] Young, Y. L., 2008, "Fluid-Structure Interaction Analysis of Flexible Composite Marine Propellers," J. Fluids Struct., **24**(6), pp. 799–818.
[12] Herath, M. T., Natarajan, S., Prusty, B. G., and St. John, N., 2014, "Smoothed Finite Element and Genetic Algorithm Based Optimization for Shape Adaptive Composite Marine Propellers," Compos. Struct., **109**(1), pp. 189–197.
[13] Maljaars, P., Kaminski, M., and deb Besten, H., 2018, "Boundary Element Modelling Aspects for the Hydro-Elastic Analysis of Flexible Marine Propellers," J. Marine Sci. Eng., **6**(2), p. 67.
[14] Triantafyllou, G. S., Triantafyllou, M. S., and Grosenbaugh, M., 1993, "Optimal Thrust Development in Oscillating Foils With Application to Fish Propulsion," J. Fluids Struct., **7**(2), pp. 205–224.
[15] Triantafyllou, M. S., Triantafyllou, G. S., and Yue, D. K. P., 2000, "Hydrodynamics of Fishlike Swimming," Annu. Rev. Fluid Mech., **32**(1), pp. 33–53.
[16] Quinn, D. B., Lauder, G. V., and Smits, A. J., 2014, "Scaling the Propulsive Performance of Heaving Flexible Panels," J. Fluid Mech., **738**, pp. 250–267.
[17] Lee, A. H., Campbell, R. L., Craven, B. A., and Hambric, S. A., 2017, "Fluid-Structure Interaction Simulation of Vortex-Induced Vibration of a Flexible Hydrofoil," ASME J. Vib. Acoust., **139**(4), p. 041001.
[18] Clark, R., Cox, D., Curtiss, H. C., Edward, J. W., Hall, K. C., Peters, D. A., Scanlan, R., Simiu, E., Sisto, F., and Strganac, T. W., 2004, *A Modern Course in Aeroelasticity: Solid Mechanics and Its Applications*, 4th ed., Springer, New York.
[19] de Langre, E., Païdoussis, M. P., Doaré, O., and Modarres-Sadeghi, Y., 2007, "Flutter of Long Flexible Cylinders in Axial Flow," J. Fluid Mech., **571**(25), pp. 371–389.
[20] Gabbai, R. D., and Benaroya, H., 2005, "An Overview of Modeling and Experiments of Vortex-Induced Vibration of Circular Cylinders," J. Sound Vib., **282**(3), pp. 576–616.
[21] Kalmbach, A., and Breuer, M., 2013, "Experimental PIV/V3V Measurements of Vortex-Induced Fluid-Structure Interaction in Turbulent Flow—A New Benchmark FSI-PfS-2a," J. Fluids Struct., **42**, pp. 369–387.
[22] Zhao, J., Leontini, J. S., Jacono, D. L., and Sheridan, J., 2014, "Fluid-Structure Interaction of a Square Cylinder at Different Angles of Attack," J. Fluid Mech., **747**, pp. 688–721.
[23] Sareen, A., Zhao, J., Lo Jacono, D., Sheridan, J., Hourigan, K., and Thompson, M. C., 2018, "Vortex-Induced Vibration of a Rotating Sphere," J. Fluid Mech., **837**(25), pp. 258–292.
[24] Campbell, R. L., and Paterson, E. G., 2011, "Fluid-Structure Interaction Analysis of Flexible Turbomachinery," J. Fluids Struct., **27**(8), pp. 1376–1391.
[25] Schmitz-Rode, T., Graf, J., Pfeffer, J. G., Buss, F., Brucker, C., and Gunther, R. W., 2005, "An Expandable Percutaneous Catheter Pump for Left Ventricular Support: Proof of Concept," J. Am. Coll. Cardiol., **45**(11), p. 1856.
[26] Throckmorton, A., Ballman, K., Myers, C., Frankel, S., Brown, J., and Rodefeld, M., 2008, "Performance of a 3-Bladed Propeller Pump to Provide Cavopulmonary Assist in the Failing Fontan Circulation," Ann. Thorac. Surg., **86**(4), pp. 1343–1347.
[27] Bhavsar, S. S., Kapadia, J. Y., Chopski, S. G., and Throckmorton, A. L., 2009, "Intravascular Mechanical Cavopulmonary Assistance for Patients With Failing Fontan Physiology," Artif. Organs, **33**(11), pp. 977–987.
[28] Throckmorton, A. L., and Kishore, R. A., 2009, "Design of a Protective Cage for an Intravascular Axial Flow Blood Pump to Mechanically Assist the Failing Fontan," Artif. Organs, **33**(8), pp. 611–621.
[29] Heil, M., and Hazel, A. L., 2011, "Fluid-Structure Interaction in Internal Physiological Flows," Annu. Rev. Fluid Mech., **43**(1), pp. 141–162.
[30] Dowell, E. H., and Hall, K. C., 2001, "Modeling of Fluid-Structure Interaction," Annu. Rev. Fluid Mech., **33**(1), pp. 445–490.
[31] Hessenthaler, A., Gaddum, N. R., Holub, O., Sinkus, R., Röhrle, O., and Nordsletten, D., 2016, "Experiment for Validation of Fluid-Structure Interaction Models and Algorithms," Int. J. Numer. Methods Biomed. Eng., **33**(9), p. e2848.
[32] Ducoin, A., Astolfi, J. A., Deniset, F., and Sigrist, J.-F., 2009, "An Experimental and Numerical Study of the Hydroelastic Behavior of an Hydrofoil in Transient Pitching Motion," First International Symposium on Marine Propulsors, Trondheim, Norway, June 22–24.
[33] Ducoin, A., Astolfi, J. A., Deniset, F., and Sigrist, J.-F., 2009, "Computational and Experimental Investigation of Flow Over a Transient Pitching Hydrofoil," Eur. J. Mech. B/Fluids, **28**(6), pp. 728–743.
[34] Derakhshandeh, J. F., Arjomandi, M., Dally, B., and Cazzolato, B., 2016, "Flow-Induced Vibration of an Elastically Mounted Airfoil Under the Influence of the Wake of a Circular Cylinder," Exp. Therm. Fluid. Sci., **74**, pp. 58–72.
[35] Gomes, J. P., and Lienhart, H., 2006, "Experimental Study on a Fluid-Structure Interaction Reference Test Case," *Fluid-Structure Interaction*, H.-J. Bungartz, and M. Schafer, eds., Springer-Verlag, Berlin, pp. 356–370.
[36] de Nayer, G., Kalmbach, A., Breuer, M., Sicklinger, S., and Wüchner, R., 2014, "Flow Past a Cylinder With a Flexible Splitter Plate: A Complementary Experimental-Numerical Investigation and a New FSI Test Case (FSI-PfS-1a)," Comput. Fluids, **99**, pp. 18–43.
[37] Deutsch, S., and Castano, J., 1986, "Microbubble Skin Friction Reduction on an Axisymmetric Body," Phys. Fluids, **29**(11), pp. 3590–3597.
[38] Fontaine, A. A., and Deutsch, S., 1992, "The Influence of the Type of Gas on the Reduction of Skin Friction Drag by Microbubble Injection," Exp. Fluids, **13**(2–3), pp. 128–136.
[39] Elbing, B. R., Daniel, L., Farsiani, Y., and Petrin, C. E., 2018, "Design and Validation of a Recirculating, High-Reynolds Number Water Tunnel," J. Fluid. Eng., **140**(8), p. 081102.
[40] Nakamura, Y., and Tomonari, Y., 1982, "The Effects of Surface Roughness on the Flow Past Circular Cylinders at High Reynolds Numbers," J. Fluid Mech., **123**, pp. 363–378.
[41] Elbing, B. R., Solomon, M. J., Perlin, M., Dowling, D. R., and Ceccio, S. L., 2011, "Flow-Induced Degradation of Drag-Reducing Polymer Solutions Within a High-Reynolds Number Turbulent Boundary Layer," J. Fluid Mech., **670**, pp. 337–364.
[42] Fahnline, J. B., Campbell, R. L., and Hambric, S. A., 2004, "Modal Analysis Using the Singular Value Decomposition," Pennsylvania State University, ARL Technical Report 04-008.
[43] Tropea, C., Scarano, F., Westerweel, J., Cavone, A. A., Meyers, J. F., Lee, J. W., and Schodl, R., 2007, "Particle Based Techniques: Laser Doppler Technique," *Handbook of Experimental Fluid Mechanics*, C. Tropea, A. L. Yarin, and J. F. Foss, eds., Springer, New York, pp. 296–309.
[44] Elbing, B. R., Young, S. D., Jonson, M. L., Campbell, R. L., Craven, B. A., Kunz, R. F., and Koudela, K. L., 2014, "Hybrid Multi-Material Rotor (HMMR) Phase 2: A Low Frequency, High Amplitude Hydrodynamic Fluid-Structure-Interaction Experiment," Pennsylvania State University, ARL Technical Report 13-004.
[45] Bendat, J. S., and Piersol, A. G., 1980, *Engineering Applications of Correlation and Spectral Analysis*, John Wiley & Sons, New York, p. 274.
[46] Pope, S. B., 2000, *Turbulent Flows*, Cambridge University Press, Cambridge, UK, pp. 147–154.
[47] Shih, W. C. L., Wang, C., Coles, D., and Roshko, A., 1993, "Experiments on Flow Past Rough Circular Cylinders at Large Reynolds Numbers," J. Wind Eng. Ind. Aerod., **49**(1–3), pp. 351–368.
[48] Bearman, P. W., 1969, "On Vortex Shedding From a Circular Cylinder in the Critical Reynolds Number Regime," J. Fluid Mech., **37**(3), pp. 577–585.
[49] Roshko, A., 1961, "Experiments on the Flow Past a Circular Cylinder at Very High Reynolds Number," J. Fluid Mech., **10**(3), pp. 345–356.
[50] Bendat, J. S., and Piersol, A. G., 1986, *Random Data: Analysis and Measurement Procedures (Second Edition, Revised and Expanded)*, John Wiley & Sons, New York, pp. 386–391.

Downloaded from http://asmedigitalcollection.asme.org/vibrationacoustics/article-pdf/142/4/041014/6527766/vib_142_4_041014.pdf by guest on 23 April 2024